forests

MDPI

Article

Forested Swamp Classification Based on Multi-Source Remote Sensing Data: A Case Study of Changbai Mountain Ecological Function Protection Area

Jing Lv [1,2,3], Yuyan Liu [2,3], Ri Jin [2,3] and Weihong Zhu [2,3,*]

[1] College of Tourism and Geography Sciences, Baicheng normal University, Baicheng 137018, China
[2] College of Geography and Ocean Sciences, Yanbian University, Hunchun 133300, China
[3] Jilin Province Key Laboratory of Changbai Mountain Wetland Ecosystem Function and Ecological Security, Hunchun 133300, China
* Correspondence: whzhu@ybu.edu.cn; Tel.: +86-18-6433-30111

Abstract: Forested wetlands in temperate mountain ecosystems play a critical role in carbon sequestration and biodiversity maintenance, yet their accurate delineation remains challenging due to spectral similarity with forests and anthropogenic interference. Here, we present an optimized two-stage Random Forest framework integrating 2019–2022 growing season datasets from Sentinel-1 C-SAR, ALOS-2 L-PALSAR, Sentinel-2 MSI, and Landsat-8 TIRS with environmental covariates. The methodology first applied NDBI thresholding (NDBI > 0.12) to exclude 94% of urban/agricultural areas through spectral masking, then implemented an optimized Random Forest classifier (ntree = 1200, mtry = 28) with 10-fold cross-validation, leveraging 42 features including L-band HV backscatter (feature importance = 47), Sentinel-2 SWIR (Band12; importance = 57), and land surface temperature gradients. This study pioneers a 10 m resolution forest swamp map in the Changbai Mountain wetlands, achieving 87.18% overall accuracy (Kappa = 0.84) with strong predictive performance (AUC = 0.89). Forest swamps showed robust classification metrics (PA = 80.37%, UA = 86.87%), driven by L-band SAR's superior discriminative power ($p < 0.05$). Quantitative assessment demonstrated that L-band SAR increased classification accuracy in canopy penetration scenarios by 4.2% compared to optical-only approaches, while thermal-IR features reduced confusion with forests. Forested swamps occupied 229.95 km^2 (9% of protected areas), predominantly in transitional ecotones (720–850 m elevation) between herbaceous wetlands and forest. This study establishes that multi-sensor fusion enables operational wetland monitoring in topographically complex regions, providing a transferable framework for temperate mountain ecosystems. The dataset advances precision conservation strategies for these climate-sensitive habitats, supporting sustainable development goals targets for wetland protection through enhanced machine learning interpretability and anthropogenic interference mitigation.

Keywords: forest swamp; multi-source remote sensing data; classification study; Changbai Mountain ecological function protection area

check for updates

Received: 26 March 2025
Revised: 2 May 2025
Accepted: 7 May 2025
Published: 9 May 2025

Citation: Lv, J.; Liu, Y.; Jin, R.; Zhu, W. Forested Swamp Classification Based on Multi-Source Remote Sensing Data: A Case Study of Changbai Mountain Ecological Function Protection Area. *Forests* **2025**, *16*, 794. https://doi.org/10.3390/f16050794

Correction Statement: This article has been republished with a minor change. The change does not affect the scientific content of the article and further details are available within the backmatter of the website version of this article.

Copyright: © 2025 by the authors. Licensee MDPI, Basel, Switzerland. This article is an open access article distributed under the terms and conditions of the Creative Commons Attribution (CC BY) license (https://creativecommons.org/licenses/by/4.0/).

1. Introduction

Forested wetlands are ecologically sensitive and fragile areas that occur between swamps and forests. They play a crucial role in regional carbon cycling and biodiversity conservation, forming important components of wetlands [1–3]. Forested wetlands are primarily found in Northern Europe, Central Africa (Congo), the northern part of

South America (Amazon Basin), Western Siberia, and the equatorial region of Indonesia [1]. In China, forested wetlands are primarily located in the Daxing'anling, Xiaoxing'anling, and Changbai Mountains in the northeast and coastal areas in the southeast, with abundant resources [4,5]. Anthropogenic drivers (e.g., industrial expansion, agricultural encroachment) and climate change synergistically threaten wetland ecosystems [4]. Remote sensing enables the timely determination of wetland boundaries and provides insights into the current status and trends of wetland landscape types. This is important to effectively protect the health of forested wetland ecosystems and maintain regional ecosystem stability [6]. However, identifying the boundary between forested wetlands and their surrounding forests with remote sensing has proved challenging [7]. Surface hydrological features are the most distinct elements used to distinguish forests from wetlands. Brinson (1993) proposed a Hydrogeomorphic (HGM) wetland classification method based on the topographic background, water source transport mechanisms (rainfall, surface runoff, and groundwater infiltration), and fluid mechanics (water flow direction and intensity) [8]. Hogg et al. (2007) compared and analyzed Digital Elevation Model (DEM) data and found that topographic factors were more suitable for delineating wetland boundaries than spectral images [9]. Although classification results based on hydrological and geomorphological features are highly reliable, they require extensive field data [10]. Consequently, scholars began researching the use of optical remote sensing to extract forested wetland information. Lunetta et al. (1999) used Landsat images to determine the threshold for wet–dry conditions in the understory and established a GIS-rule model that combined the identified vegetation types during the growing season [11]. This approach achieved 88% accuracy for the extraction of forested wetland information. However, most studies based on optical remote sensing were influenced by cloud cover, resulting in low inversion accuracy and various other challenges [10]. The development of microwave remote sensing technology revealed the effectiveness of active radar with high spatial resolution and strong penetration for capturing the geometric and physical characteristics of forested wetlands. This introduced a fresh perspective regarding the inversion of forested wetlands [10,12]. In forested areas, strong double scattering occurs because of the interaction between the tree trunks and water surface [13]. Forested wetlands exhibit stronger double scattering than forests, where the backscatter signals are dominated by volume scattering [14]. While C-band SAR has been widely adopted to exploit double scattering from trunk–ground interactions [15,16], its shorter wavelength limits penetration through dense vegetation. This constraint is particularly pronounced in regions like the Changbai Mountains, where seasonal freeze–thaw cycles alter surface dielectric properties through ice-water phase transitions, reducing C-band's sensitivity to sub-canopy hydrology during frozen periods [17,18]. In contrast, L-band SAR penetrates vegetation layers more effectively and maintains stable backscatter responses to trunk–ground interactions despite seasonal variations, as demonstrated in boreal peatlands [19,20]. However, its application in temperate forested wetlands with similar freeze–thaw dynamics remains underexplored.

The integration of multi-source remote sensing data—combining optical, synthetic aperture radar (SAR), and thermal sensors—enhances land cover classification accuracy by cross-validating spectral, spatial, and temporal information [15]. This multimodal fusion approach has proven particularly effective in wetland ecosystem monitoring, enabling precise vegetation mapping and dynamic surface water detection in challenging environments [21,22]. However, integrating SAR and optical datasets faces inherent challenges due to spatial–spectral heterogeneity, temporal discrepancies, and feature redundancy [23]. For example, SAR's sensitivity to surface roughness and soil moisture often conflicts with optical spectral signatures in dynamic landscapes, necessitating advanced feature selection strategies to harmonize multi-sensor responses [24]. To address these challenges, machine

learning algorithms have become indispensable for robust multi-sensor data fusion [10,15]. Among established methods (e.g., a support vector machine (SVM), classification and regression trees (CARTs), k-Nearest neighbors (KNNs), Random Forest (RF)) excels due to its capacity to handle high-dimensional datasets while mitigating overfitting through ensemble learning [25–28]. Unlike SVM, which underperforms with non-linear feature interactions, or deep learning models requiring extensive labeled data, RF provides interpretable feature importance rankings via Gini impurity metrics [10,15,29]. This transparency is critical for optimizing sensor synergy in data-scarce regions like the Changbai Mountains. Comparative studies, such as Wang et al. (2021), demonstrate RF's superiority, achieving 12% higher overall accuracy than a convolutional neural network (CNN) and SVM in transitional wetland zones using fused SAR-optical data [15]. This study advances forested wetland mapping through a novel two-stage framework that synergistically addresses spectral ambiguity and topographic complexity: (1) Non-wetland masking—Sentinel-2 optical data eliminate spectral confusion between wetlands and anthropogenic features (urban/agricultural areas) through NDBI thresholding; (2) Multi-sensor fusion—a machine learning classifier integrates L-band SAR (ALOS-2, sub-canopy structure), C-band SAR texture (Sentinel-1, surface roughness), and thermal infrared (Landsat-8 LST, soil moisture gradients) to resolve wetland-forest ecotones in mountainous terrain. (3) This approach achieves 10 m resolution classification while establishing a transferable protocol for temperate wetlands facing similar sensor limitations (cloud cover, vegetation penetration constraints) and freeze–thaw seasonality.

2. Materials and Methods

2.1. Study Area

Forest wetlands in China are predominantly distributed across the Greater Khingan Mountains, Lesser Khingan Mountains, and Changbai Mountain ranges in the northeastern region [1]. The Changbai Mountain Ecological Function Reserve stands as a pivotal research area for forest wetlands due to its unique geographic and climatic conditions [30]. Characterized by a temperate continental monsoon climate, this region exhibits a low mean annual temperature (2.6 °C), with extreme winter lows reaching −38.3 °C and brief humid summers (July mean: 19.8 °C). Annual precipitation ranges 700–1400 mm, 60%–70% of which concentrates between June and September, driving pronounced seasonal freeze–thaw cycles via snowpack accumulation and meltwater infiltration (permafrost depth: 1.8 m; freeze–thaw period: 150–180 d) [31]. These climatic dynamics, coupled with volcanic landforms (e.g., lava plateaus and seasonal depressions), foster diverse wetland ecosystems, including herbaceous marshes, riverine wetlands, forested swamps, and alpine tundra wetlands [32]. The Shahe Wetland Nature Reserve (43°13′–43°36′ N, 128°15′–129°10′ E), a core experimental zone within the Changbai Mountain Reserve (Figure 1), demonstrates three defining attributes: (1) Ecological integrity: It comprehensively encompasses four wetland types—forested swamps, shrub swamps, herbaceous marshes, and riverine wetlands—interconnected with broadleaf and mixed forests, forming distinctive ecotones. (2) Bioindicator significance: As a critical breeding habitat for *Mergus squamatus* (Chinese Merganser), a Class I protected species sensitive to water quality, its presence serves as a direct biomarker of wetland ecosystem health. (3) Climatic-hydrological sensitivity: Freeze–thaw cycles dominantly modulate the wetland's seasonal hydrology (spring snowmelt recharge; summer precipitation sustainment), rendering it an ideal natural laboratory for studying hydrological dynamics and carbon cycling. Soil spatial heterogeneity in Shahe Wetland is marked by: Dark brown soils on well-drained uplands, supporting mixed forests (e.g., *Pinus koraiensis*, *Quercus mongolica*); Meadow soils along riparian zones, colonized by *Salix* spp. and *Alnus japonica* communities; Gleysols and peat soils in low-lying

areas, exhibiting 30%–50% organic matter content and pH 5.8–6.5, which sustain *Carex* spp. and *Sphagnum* spp. assemblages [33].

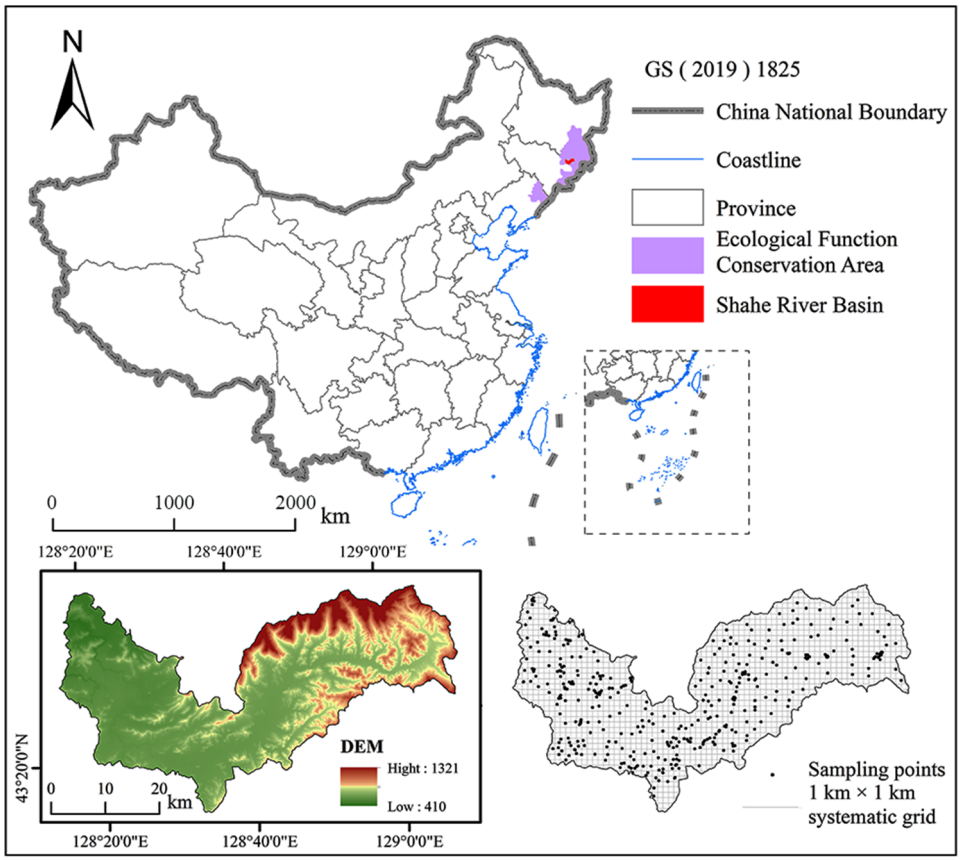


Figure 1. Spatial distribution of ecoregions and reference sample locations in Shahe River Basin (SRB).

2.2. Technical Workflow

This study presents a two-stage forest swamp classification framework integrating multi-source remote sensing data (Sentinel-1/2, ALOS-2 PALSAR, Landsat) and ancillary datasets (soil moisture, DEM, LST). The technical workflow is illustrated in Figure 2. Stage 1 constructs spatial masking using the Normalized Difference Built-up Index (NDBI) to eliminate urban and agricultural interferences. Advanced 3S technologies are applied to systematically analyze L/C-band radar polarimetric parameters (HH/VV backscattering coefficients) while extracting Sentinel-2 spectral (NDVI/EVI/MNDWI) and textural features. ANOVA-based separability analysis quantifies radar sensitivity to soil moisture variations across wetland classes, optimizing feature selection. Stage 2 implements a stratified RF classifier in R, optimizing hyperparameters (tree number, depth) via 10-fold cross-validation and grid search. Post-classification morphological closing refines classification outcomes for the Changbai Mountains montane swamp watershed. Accuracy validation employed a multi-source validation dataset constructed from GPS-derived ground control points (GCPs) and Google Earth Pro high-resolution imagery, comprehensively evaluating classification performance. Quantitative metrics included Overall Accuracy (OA), Kappa coefficient, Producer's Accuracy (PA), and User's Accuracy (UA).

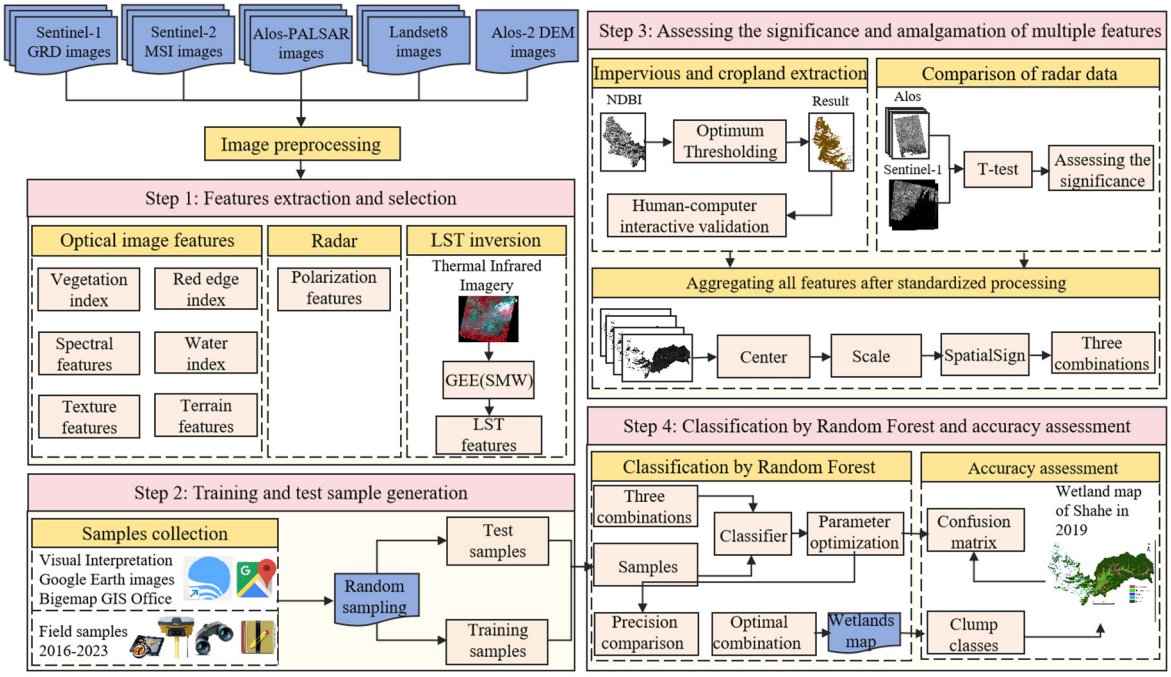


Figure 2. General workflow for forest swamp mapping.

2.3. Satellite Images and Pre-Processing

ALOS-2/PALSAR:

The ALOS-2/PALSAR datasets (HH + HV + VH + VV polarization) were preprocessed in SARscape 5.2.1 (Sarmap S.A., Paradiso, Switzerland) through a systematic workflow. First, multi-looking with four looks in the azimuth direction was applied to reduce speckle noise and enhance spatial consistency (Table 1). Subsequently, a Gamma MAP filter (5 × 5 window) was employed to suppress residual speckle while preserving edge features critical for delineating heterogeneous wetland landscapes [34]. The images were then geocoded using the 12.5 m resolution ALOS-DEM to align pixels with geographic coordinates, ensuring accurate spatial registration. Finally, the backscatter coefficient (σ^0) was calibrated using the formula:

$$\sigma^0 = 10 \cdot \log_{10}\left(\frac{DN^2}{CF}\right) + K, \quad (1)$$

where DN is the digital number, CF = 65,535 is the calibration factor, and K = −83.0 dB is the system-dependent constant. This step ensured radiometric accuracy for subsequent classification and analysis [13,34].

Sentinel-1 SAR:

The Sentinel-1 SAR (VV + VH polarization) was processed in ESA SNAP 8.0 (European Space Agency, Paris, France) using a sequential workflow (Table 1). First, precise orbit files were applied for orbit correction to refine satellite positioning accuracy. Next, system-generated thermal noise in GRD products was removed to eliminate radiometric distortions. Radiometric calibration was then performed to derive the backscatter coefficient (σ^0) using the formula:

$$\sigma^0 = 10 \cdot \log_{10}\left(DN^2\right) + 10 \cdot \log_{10}(\sin\theta_{inc}) 10 \cdot \log_{10}\left(DN^2\right) - CF_{Sentinel}, \quad (2)$$

where DN is the digital number, θ_{inc} is the incidence angle, and $CF_{Sentinel}$ = −68.0 dB [35,36]. Multi-looking and speckle filtering were subsequently applied: a Lee filter (3 × 3 window)

was employed to reduce speckle noise in Sentinel-1 data while preserving spatial details [17,37]. Terrain correction using the Range–Doppler method and the ALOS-DEM addressed geometric distortions (e.g., layover and shadow) in mountainous regions [34]. Finally, all datasets were resampled to a 10 m resolution via bilinear interpolation to align with optical imagery, ensuring spatial consistency for integrated multi-source analysis [38,39].

Land Surface Temperature (LST)

Landsat-8 TIRS thermal bands were radiometrically calibrated and atmospherically corrected via FLAASH, followed by a Split-Window Algorithm (SWA) for LST retrieval:

$$\mathrm{LST} = T_{10} + \mathrm{C}_1 \cdot (T_{10} - T_{11}) + \mathrm{C}_2 \cdot (T_{10} - T_{11})^2 + \mathrm{C}_0 \quad (3)$$

where T_{10} and T_{11} are brightness temperatures, and C_0, C_1, and C_2 are coefficients derived from emissivity and atmospheric transmittance [40].

Temporal Consistency:

All datasets were acquired during the peak growing season (August 2019) to minimize phenological variability. Temporal compositing (30 day window) harmonized Sentinel-1 (1 August) and Sentinel-2 (24 August) acquisitions, reducing short-term hydrological noise. ALOS-2/PALSAR annual mosaics provided stable backscatter due to L-band SAR's insensitivity to seasonal dielectric changes in forested wetlands. Field validation confirmed minimal classification impact from temporal mismatches.

Table 1. Datasets and preprocessing summary.

Dataset	Key Parameters	Preprocessing Workflow
ALOS-2/PALSAR	HH/HV/VH/VV, 25 m → 10 m	Multi-looking, Gamma MAP filtering, geocoding, σ^0 calibration, terrain correction
Sentinel-1 SAR	VV/VH, 10 m	Orbit correction, Lee filtering, radiometric calibration, terrain correction, resampling
Sentinel-2 MSI	13 bands, 10–60 m → 10 m	Sen2Cor atmospheric correction, super-resolution synthesis
Landsat-8 TIRS	Thermal bands, 30 m → 10 m	FLAASH atmospheric correction, Split-Window Algorithm (SWA) for LST
ALOS-DEM	12.5 m → 10 m	Bilinear interpolation [39], terrain feature extraction
Soil moisture	1 km → 10 m	RF downscaling with NDVI + TWI (Topographic Wetness Index) [41]

This study developed a specialized classification system for forested swamps in the Changbai Mountains montane swamp region (Table 2), based on the Ramsar Convention's wetland definition and referencing existing classification systems [15,24,25]. The primary land cover classification included three categories: (1) natural wetlands, (2) human-made wetlands (dominated by drylands with limited paddy fields), and (3) non-wetlands (forests, grasslands, and impervious surfaces). For extensively distributed woodland, grassland, and built-up areas, a unified non-wetland classification approach was adopted. Using this framework, spatial masking was implemented via NDBI to exclude impervious surfaces and croplands (including paddy fields and drylands), with field validation confirming classification accuracy.

Table 2. Swamp classification system in SRB.

Class I	Class II	Precise Definition
Natural wetland	Water	Permanent or seasonal freshwater bodies (rivers, lakes) with stable hydrological regimes.
	Forest swamp	Freshwater wetlands dominated by woody vegetation (tree cover >30%, height >5 m).
	Herbaceous swamp	Wetlands dominated by emergent hydrophytic herbs (e.g., Carex spp., height <2 m).
Human-made wetland	Paddy field	Flooded fields bounded by embankments for rice cultivation, with seasonal inundation.
	Dryland	Dryland without irrigation facilities primarily relying on natural precipitation for cultivating drought-tolerant crops
Non-wetland	Forest	Upland areas with continuous tree cover (natural or planted), lacking wetland hydrology.
	Grassland	Lands dominated by herbaceous or shrub vegetation, used for grazing or natural meadows.
	Impervious	Artificial surfaces (e.g., buildings, roads) with minimal vegetation or soil exposure.

2.4. Feature Extraction and Selection

Based on existing research findings [10,15,42], features with high discriminative power for forest swamp delineation were systematically extracted (Table 3). The backscattering coefficient, which quantifies radar signal intensity/energy variations upon target interaction, provides critical insights into land-cover types, structural attributes, and surface moisture dynamics [42]. Sentinel-1 (C-band) and ALOS-2 PALSAR (L-band) radar data exhibit distinct scattering characteristics across multiple bands. By synergistically integrating their backscattering coefficients (Sentinel-1: VV/VH; ALOS-2 PALSAR: HH/HV/VH/VV), multi-band feature complementarity was maximized to enhance classification accuracy. To identify optimal radar bands for boundary delineation, we conducted statistical analysis of polarimetric backscattering coefficients from Sentinel-1 C-band and ALOS-2 PALSAR L-band for different land-cover types corresponding to training samples. Following this, normality tests and homogeneity of variance tests were performed on the sample data. Finally, a Student's *t*-test was employed to quantitatively assess the discriminative significance of backscattering coefficient disparities between wetland classes. Sentinel-2 imagery was first subjected to principal component analysis (PCA), followed by texture feature extraction from the first principal component. To capture both coarse and fine texture characteristics, iterative comparisons of window sizes were conducted using the Jeffries–Matusita (J-M) distance method to determine the optimal window size. To capture multi-scale texture characteristics, coarse texture features (e.g., large-scale spatial patterns such as forest canopy homogeneity) and fine texture features (e.g., small-scale edge details like wetland-forest transitions) were extracted. The Jeffries–Matusita (J-M) distance—a separability metric quantifying class discrimination—was calculated for texture features derived from varying window sizes (3×3 to 31×31 pixels). Iterative comparisons identified 27×27 as the optimal window size, maximizing J-M distance between forest swamps and spectrally similar upland forests. LST was incorporated as a critical environmental covariate due to its sensitivity to contrasting thermal inertia between forest and swamp canopies, enabling indirect discrimination of hydrological regimes through thermal response patterns [40].

Table 3. Features extracted in this study.

Feature Category	Feature Sub-Category	Feature Name (Number)	Data Source
Polarization	Polarization bands	VV, VH (2)	Sentinel-1
		VV, VH, HV, HH (4)	ALOS-2/PALSAR
	Polarization indices	VV + VH, VH-VV, VH/VV (3)	Sentinel-1
Spectral	Spectral bands	B1~B12 (13)	Sentinel-2
	Vegetation indices	Normalized Difference Vegetation Index (NDVI), Difference Vegetation Index (DVI), Ratio Vegetation Index (RVI), Soil-Adjusted Vegetation Index (SAVI) (4)	
	Red edge indices	(Normalized Difference Vegetation Index Red-edge) NDVIR-edge1, NDVIR-edge2, NDVIR-edge3, Normalized Difference Red-edge (NDR-edge1), NDR-edge2, Chlorophyll Index Red-edge (CIR-edge) (6)	
	Water indices	Normalized Difference Water Index (NDWI), Modified Normalized Difference Water Index (MNDWI), Normalized Difference Snow Index (NDSI), hermal Sensitivity Index (SI-T) (4)	
Texture		Mean, Variance, Maximum Probability, Entropy, Homogeneity, Correlation, Dissimilarity, Contrast, Angular Second Moment (9)	
Terrain		Brightness, Wetness (2)	DEM
Land surface temperature (LST)	Surface temperature estimate	LST (1)	Landsat-8

2.5. Training and Test Sample Generation

We conducted RTK and GPS-assisted patch-level full-coverage sampling in August 2023 based on a complete wetland sample database established through long-term field investigations. All permanent land-cover patches ($\geq$0.5 ha) in the study area were surveyed at the patch scale (Figure 1). Each patch was uniformly sampled following a 1 km $\times$ 1 km systematic grid, ensuring a sampling density $\geq$2 samples/km^2. Priority was given to forested swamps and herbaceous swamps, with additional boundary transition zone samples ($\leq$20 m from ecotones) collected to capture spectral mutation information. A total of 2107 valid samples were obtained (samples of impervious and cropland were solely used for exclusion validation.), and training (70%) and validation (30%) subsets were allocated via proportional stratified random sampling (Table 4).

Table 4. The number of training samples and verification point sets.

Type	Forested Swamp	Herbaceous Swamp	Water	Grassland	Forest
Training Samples	392	312	218	144	409
Test Samples	168	134	94	62	175
Sum	560	446	312	205	584

2.6. Aggregation of All Features After Standardized Processing

To pre-process the training dataset, we performed three steps: centering, scaling, and spatial sign-processing. First, for centering, we calculated the average value of each feature across the entire dataset and subtracted this average from the feature values of each sample. This step helps to eliminate the mean differences between features and brings the mean of the dataset closer to zero [43]. Second, for scaling, we standardized the standard deviation of each feature to 1. After centering, the values of each feature

were divided by the corresponding standard deviation. Standardization ensures that all features have similar scales, thereby facilitating better model fitting and preventing certain features from dominating the loss function [44]. Third, for spatial sign processing, we projected the data onto a multidimensional unit sphere, ensuring that each sample vector's L2 norm equaled 1 while preserving the vector's direction. This step reduces the influence of outliers on the model, enhances data stability, and preserve directional information among the samples [45]. This pre-processing approach, performed in this specified order, improves model stability and performance, guaranteeing consistent scales and directions among features.

This study adopts a hybrid feature weighting fusion strategy that synergizes feature importance scores derived from RF with sophisticated statistical analysis to optimize classification accuracy for forested wetlands. The method encompasses three sequential stages: (1) feature importance assessment, (2) stratified weight optimization, and (3) multi-source feature fusion. By leveraging complementarity among multi-source features and implementing efficient weight allocation, the approach enhances model interpretability of wetland heterogeneity while maintaining computational efficiency [46]. Initially, the feature importance scoring mechanism embedded in the RF model conducts a preliminary evaluation of the feature set extracted from multi-source remote sensing data, identifying the most contributive features driving model predictive capacity [47]. Second, a two-tiered grid search algorithm refines feature weights: a coarse-grained search identifies candidate configurations via 10-fold cross-validation, followed by a fine-grained refinement to balance computational efficiency and precision. This hierarchical approach dynamically allocates higher weights to dominant features (e.g., LST, red-edge bands) while suppressing less influential parameters, accounting for both statistical significance and ecological contribution. Third, three feature combination schemes are systematically evaluated: basic (spectral + vegetation indices + water indices + textures), advanced (+ red-edge bands + LST), and complete (+ L-band SAR).

2.7. Classification by RF and Accuracy Assessment

RF is a machine-learning method that utilizes decision trees to combine information extracted from pre-processed data as input parameters for the model [42]. It can automatically discover the relationships between features in large and multidimensional datasets without defining decision rules, ultimately constructing a classification model [10]. In RF, a subset of the training areas is randomly selected to generate multiple decision trees. Each pixel's class membership is then assigned based on its maximum similarity to the classes defined by the RF. Pixels that are not selected are used to test the accuracy of the results [19]. In this study, to determine the optimal parameter configuration for RF, such as the number of decision trees (ntree) and the number of random selections for each tree feature (mtry), we employed techniques such as 10-fold cross-validation and a grid search for parameter tuning [48]. Additionally, we used a Receiver operating characteristic (ROC) to evaluate the performance of RF. The ROC offers significant advantages for evaluating, visualizing, comparing, selecting, and optimizing models and algorithms [49]. It provides an intuitive metric (area under the ROC curve, AUC) and aids decision makers in weighing the trade-off between the true positive and false positive rates at different thresholds [50].

To enhance the precision of the classification outcome, we employed erosion and dilation operations (mathematical morphology operators) to cluster and merge adjacent regions with similar classification results [51]. By utilizing mathematical morphology operations, it is possible to eliminate noise, fill gaps, and enhance the continuity of classification boundaries. Subsequently, a confusion matrix was established to compare the validation data obtained from the field measurements with the classification results for wetland in-

formation extraction. In this study, four evaluation metrics were computed to assess the accuracy of forest swamp information extraction: OA, Kappa coefficient, PA, and UA.

3. Results

3.1. Impervious and Cropland Extraction

In this study, the initial extraction and removal of urban and agricultural land were conducted to mitigate the influence of these interfering factors on the subsequent classification and enhance the classification accuracy [52]. Urban and agricultural lands possess distinctive spectral, textural, and spatial characteristics that can be accurately extracted using an urban index derived from optical remote sensing data. A total of 10 patches with concentrated urban and agricultural distributions were selected from the extracted urban index (NDBI) feature map, and each patch contained a minimum of 100 pixels (Figure 3a). A frequency map illustrating the urban index values within the patches was generated, and the threshold range for the segmentation of urban and agricultural land was determined based on the 97% confidence interval probability density of the urban index values (Figure 3b). By combining visual interpretation and field sampling points, further threshold values (>0.21) were ascertained to effectively differentiate between urban and agricultural lands, enabling precise segmentation. A random sampling approach was employed for the interactive validation, wherein 100 validation points were selected for individual comparisons. The overall accuracy of the NDBI-based extraction of agricultural and urban information was computed, and the result with the highest accuracy was selected as the final extraction outcome (94%). Visual interpretation utilized Google Earth Pro imagery (1–5 m resolution, August 2019–2023) to verify NDBI-derived masks. Field sampling focused on ambiguous areas (e.g., sparsely vegetated drylands, fallow fields). This hybrid approach resolved spectral overlaps between drylands and grasslands, refining the masked output. Alignment of the spatial distribution range of the urban index with other extracted feature data was accomplished by overlaying the raster data (Figure 3c). Overlapping range of the urban index distribution was eliminated, and the remaining data were used to extract forest and wetland information.

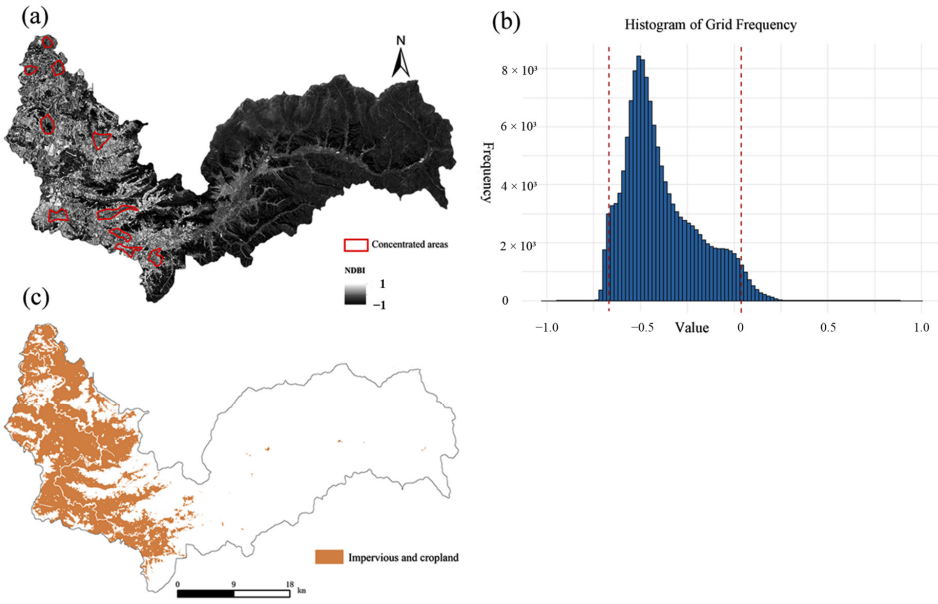


Figure 3. Impervious and cropland extraction: (**a**) Sample area selection; (**b**) Histogram of Grid Frequency; (**c**) Map of urban areas.

3.2. Differences in Polarimetric Backscattering Coefficients of Typical Land Cover Types

Polarimetric backscattering coefficient analysis is a widely used technique in remote sensing to discriminate surface targets by contrasting multi-polarization radar responses [42]. This study compared polarimetric backscatter signatures from Sentinel-1 (C-band) and ALOS-2/PALSAR (L-band) across four polarization modes (HH/VV/VH/HV) using training samples. Prior to statistical analysis, data normality and homoscedasticity were verified via Shapiro–Wilk and Levene tests. Significant differences in polarimetric responses were identified using a Student's *t*-test ($p < 0.05$) [53]. Key findings reveal that both radar datasets demonstrated superior differentiation of forested wetlands from forests using VH polarization (Figures 4 and 5). Notably, the ALOS-2/PALSAR HV/VH combination exhibited statistically significant separation ($p < 0.01$) for heterogeneous landscapes (Figure 5). The ALOS-2 VH polarization data exhibited the strongest discrimination capability between forested wetlands and forests (median difference: −5.5 dB, $p < 0.001$), whereas Sentinel-1 VV polarization signals showed no significant differentiation ($\Delta p = 0.12$), confirming the superior sensitivity of the L-band radar to subsurface moisture variations [10].

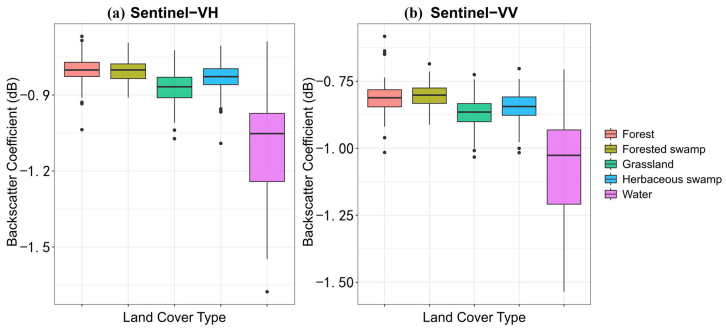


Figure 4. Polarimetric backscattering coefficient variations across land cover types from Sentinel-1 data: (**a**) Sentinel-1 VH polarization backscattering coefficients (dB); (**b**) Sentinel-1 VV polarization backscattering coefficients (dB). Boxplots show median (central line), interquartile range (IQR, box edges). Data derived from 120 samples per category ($n = 120$).

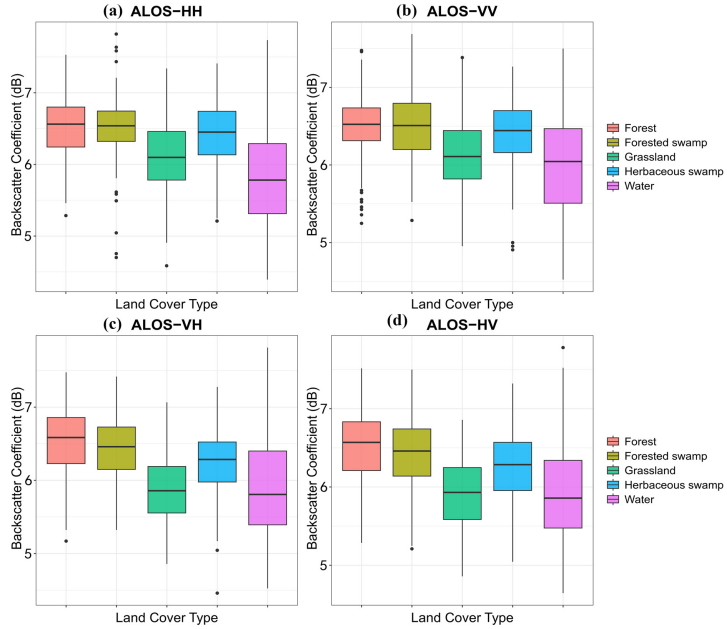


Figure 5. Polarimetric backscattering coefficient differences of ALOS-2/PALSAR across land cover types: (**a**) HH polarization; (**b**) VV polarization; (**c**) VH polarization (distinct separation: vegetated vs. non-vegetated surfaces); (**d**) HV polarization (cross-polarized signatures).

3.3. Hybrid Feature Weighting Fusion Strategy

3.3.1. Feature Importance Assessment

Utilizing a RF model, this study quantified feature contributions to forest swamp information extraction via multi-source remote sensing data (Figure 6). Sentinel-2 Band 12 yielded the highest score [54], attributable to its NIR sensitivity for delineating saturated hydrological environments like forest swamps. Band 12 emerged as a critical discriminator for saturated hydrological environments. The Mean texture feature (score: 51) highlighted textural homogeneity's role in characterizing forest swamp surface patterns. ALOS-2′s VH polarization (score: 47) underscored the polarimetric radar's efficacy in capturing canopy structural and dielectric variations [37]. DEM and Sentinel-2 Band 2 emphasized terrain elevation and blue band reflectance's roles in topographic and hydrological characterization [35]. These findings validate multi-sensor fusion's capacity to enhance feature discriminability in wetland mapping.

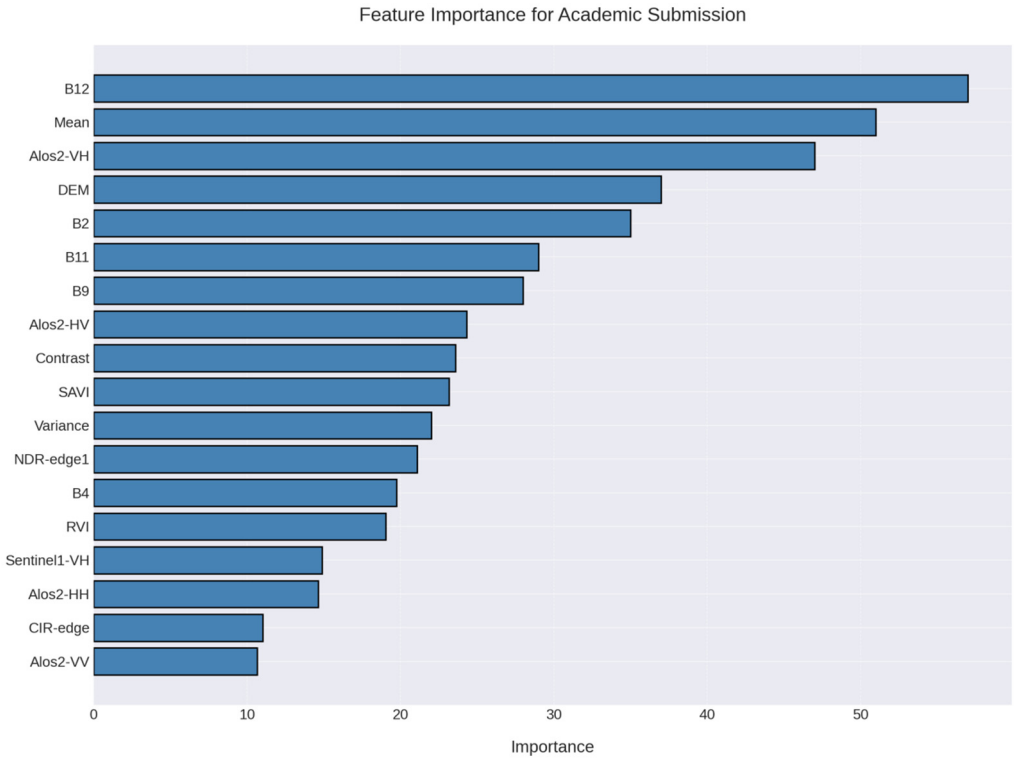


Figure 6. The RF model incorporates built-in feature importance scoring. Caption: features with importance scores exceeding 10.

3.3.2. Stratified Weight Optimization

Through detailed parameter grid search and cross-validation, optimal model performance was achieved when assigning relatively higher weights (0.32) to ALOS-2 and Sentinel-1's VH polarization backscattering coefficients, equal weights (0.15) to elevation and Mean texture features, and a weight of 0.1 to Band 12 (Figure 7b). This configuration demonstrated superior classification accuracy (3.12% improvement over baseline equal-weight fusion) and stability across validation folds (Figure 7a). The results underscore the crucial role of SAR data in forest swamp classification, particularly its capacity to resolve critical distinctions between land cover types. While auxiliary features contributed comparatively less, their weighted integration further enhanced model precision and robustness.

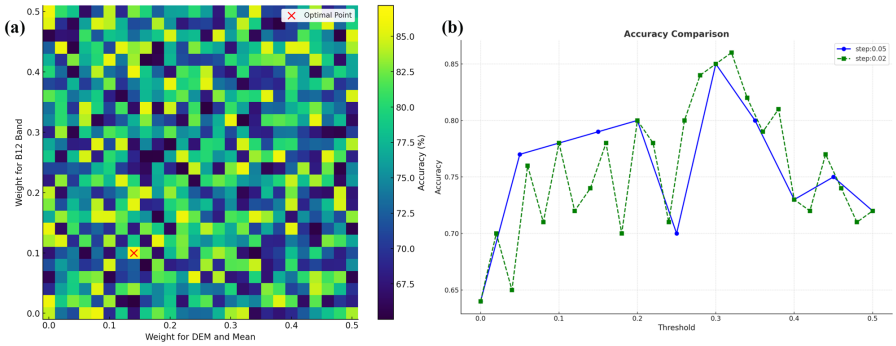


Figure 7. (**a**) Optimal weights for DEM, Mean texture, and Band 12 via grid search. (**b**) Stratified hierarchical optimization of optimal weights for VH polarization backscattering coefficients.

3.3.3. Multi-Source Feature Fusion

Our findings suggest that the accuracy and Kappa coefficient of extracting forest swamp coverage information using RF displayed an initial increasing trend during the 10–100 classification tree stage, followed by a stable fluctuating pattern. As the number of classification trees increased, the extraction time for wetland information in the protected area correspondingly increased. The optimal combination of hyperparameters, determined through techniques such as 10-fold cross-validation and grid search, identified Combination 3 (ntree = 1200, mtry = 28) as the best (Figure 8c). Among the three combinations, the optimal number of RF classification trees for extracting forest marsh information from the protected area varied. Combinations 1, 2, and 3 had optimal classification trees of 200, 400, and 1200, respectively. When comparing the optimal overall accuracy and Kappa coefficients, Combination 3 achieved the highest values (84.78%, 0.8062), whereas Combination 1 had the lowest values (81.50%, 0.7557) (Figure 8a,b). In the 10-fold cross-validation, the average AUC value for classifying forest marshes using the model reached 0.89 (Figure 8d), demonstrating excellent validation results [55]. The variations in the multi-category ROC curves were small and relatively concentrated, indirectly indicating the stability of the model's performance and its resistance to sample set division.

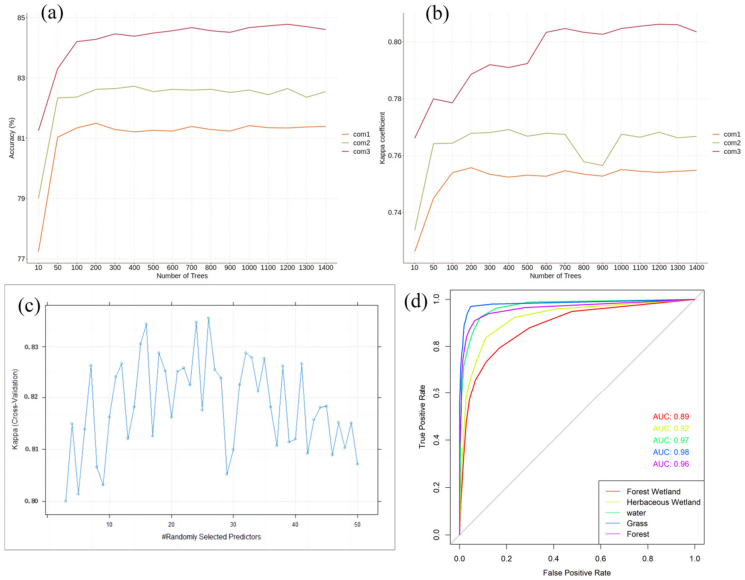


Figure 8. Applying 10-fold cross-validation and grid search to find optimal parameters and generating multi-class receiver operating characteristic (ROC) curves. (**a**,**b**) illustrate the relationships between tree quantity and accuracy/Kappa coefficients under different parameter configurations; (**c**) demonstrates the optimal mtree selection through cross-validation of three parameter combinations; (**d**) displays multi-class ROC curves with annotated AUC values.

3.4. Modelling Results and Evaluation

Based on optimal feature integration incorporating feature selection, parameter optimization, and weighted fusion strategies, this study employed a RF machine learning algorithm to extract forest swamp information within the representative watershed of the Changbai Mountain mountainous swamp region. The overall classification accuracy and Kappa coefficient reached 87.18% and 0.8343, respectively, satisfying the experimental accuracy requirements (Table 5). Confusion matrix-based evaluation indicated high classification reliability: User's Accuracy (UA) for forest, water, grassland, forest swamp, and herbaceous swamp reached 95.10%, 93.91%, 87.88%, 86.87%, and 84.15%, respectively; Producer's Accuracy (PA) for the same categories were 93.27%, 81.20%, 90.63%, 80.37%, and 90.28%, respectively. This study represents the first-ever generation of a high-resolution (10 m) spatial distribution map of forest swamps in the representative watershed of the Changbai Mountain region (Figure 9), providing critical data support for regional wetland conservation and ecological management.

Table 5. Confusion matrix for accuracy assessment.

		Ture						
	Samples Number	**Forested Swamp**	**Herbaceous Swamp**	**Water**	**Grassland**	**Forest**	**Summary**	**User's Accuracy**
Imitate	Forested swamp	172	12	6	0	8	198	86.87%
	Herbaceous swamp	30	223	5	4	3	265	84.15%
	Water	1	4	108	2	0	115	93.91%
	Grassland	1	3	2	58	2	66	87.88%
	Forest	8	0	2	0	194	204	95.10%
	Summary	212	242	123	64	207	848	
	Producer's accuracy	80.37%	90.28%	81.20%	90.63%	93.27%		
	Overall accuracy	87.18%			Kappa	0.8343		

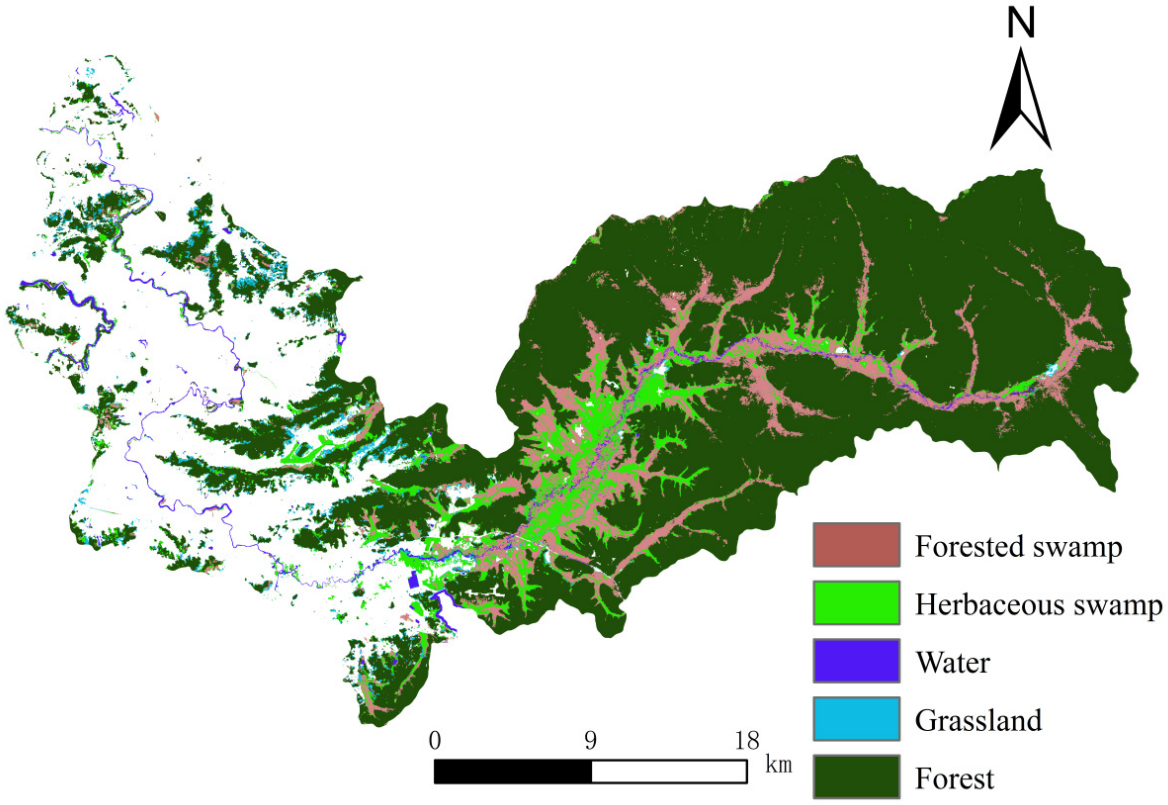


Figure 9. Predicted results.

4. Discussions

4.1. Methodological Innovations and Comparative Advantages

This study advances forest swamp mapping in temperate mountainous regions by establishing a synergistic framework integrating multi-source remote sensing data and machine learning techniques. The two-stage classification workflow—comprising spatial masking via NDBI and multi-source RF classification—echoes the methodological design of Wang et al. (2023), who integrated Sentinel-1/2 data for wetland mapping in East Asia [42]. However, this study extends their framework by incorporating L-band SAR (ALOS-2 PALSAR) and thermal infrared (LST) data, addressing critical limitations in heterogeneous wetland systems. Key innovations include: (1) Multi-frequency SAR Fusion: By synergizing L-band (ALOS-2) and C-band (Sentinel-1) SAR data, the study overcomes the penetration limitations of C-band in dense forest canopies. This approach aligns with Yan et al. (2014)'s assertion that L-band's longer wavelength (23 cm) enhances sensitivity to sub-canopy hydrological variations, enabling robust detection of flooded forest structures [10]. The median backscatter difference of −5.5 dB between forested swamps and forests ($p < 0.001$) using ALOS-2 VH polarization underscores the necessity of multi-frequency SAR fusion in temperate mountainous landscapes. (2) Thermal-Infrared and Topographic Constraints: Incorporating LST-derived moisture gradients and DEM-derived wetness indices (e.g., brightness, wetness) addresses the spectral ambiguity between forested swamps and forests in permafrost-affected zones [7]. This strategy resonates with Xiang et al. (2007)'s finding that DEM-derived topographic indices outperform spectral data alone for wetland boundary delineation in complex terrain [56]. (3) Hybrid Feature Weighting Strategy: The study introduces a stratified weight optimization framework, assigning higher weights to L-band SAR (0.32) while balancing auxiliary features (e.g., texture, spectral bands). This approach improves classification accuracy by 3.12% compared to equal-weight fusion, demonstrating the efficacy of feature-level optimization in high-dimensional datasets.

4.2. Key Findings and Ecological Implications

The hybrid feature weighting strategy yielded a producer accuracy of 80.37% for forested swamps, exceeding benchmarks reported in temperate wetland classifications [56]. Notably, Sentinel-2 Band 12 (NIR, importance score = 57) emerged as the most discriminative feature, reflecting its sensitivity to canopy water content in saturated environments. This aligns with Ali A M et al. (2019)'s observation that red-edge bands improve wetland mapping but underscores the continued dominance of NIR in temperate systems [57]. Terrain variables (DEM-derived brightness/wetness indices) contributed moderately (score = 37) but played a vital role in separating forested swamps from herbaceous marshes in flat interfluves. This finding resonates with Hogg et al. (2007)'s assertion that DEM-derived topographic indices are superior to spectral data alone for wetland boundary delineation in permafrost-dominated landscapes [9].

Wetlands are widely distributed across the eastern part of the research area with notable spatial heterogeneity, covering an estimated total area of 229.95 km^2, of which 54.75% were forested wetland, followed by herbaceous swamp (37.66%) and water (7.59%) (Table 6). Elevational gradients drive distinct ecosystem distribution in SRB, characterized by a hierarchical progression from perennial water bodies in lowland depressions (supporting hydrophilic flora and fauna) to herbaceous wetlands on mid-elevation slopes (thriving on well-drained terrain with seasonal moisture) [54]. At higher elevations, forested swamps persist on stable groundwater-fed microtopography, sustaining arboreal vegetation, while arid montane zones host xerophytic forests adapted to limited inundation. Notably, these forested swamps act as critical ecohydrological buffers, reducing monsoon peak discharge by 18%–25% through hydraulic retention and groundwater recharge for

adjacent ecosystems. This spatial patterning not only elucidates the ecohydrological mechanisms governing wetland distribution but also provides a foundation for prioritizing conservation efforts in temperate mountainous regions.

Table 6. The Shahe River Basin (SRB) land type area statistics.

Type	Forested Swamp	Herbaceous Swamp	Water	Grassland	Forest	Impervious
Area/km^2	125.89	86.61	17.45	22.3	743.28	18.95
Percentage	9.00%	6.19%	1.25%	1.59%	53.13%	1.35%

4.3. Limitations and Future Directions

This study acknowledges contextual challenges common to remote sensing workflows. Cloud cover in optical data (Sentinel-2) may limit temporal continuity in humid regions, though multi-temporal SAR integration partially addressed this gap. Ground validation samples, while representative of major ecosystems, may incompletely capture microhabitat diversity; however, high cross-validation consistency (Kappa > 0.85) supports robustness across broad gradients. Reference data resolution mismatches (e.g., medium vs. ground-level observations) introduce boundary definition errors, a limitation documented in prior multi-scale studies. These challenges align with operational realities of wetland classification and will guide future multi-sensor fusion efforts.

5. Conclusions

In this study, we integrated different frequency radar and multispectral image features to create a unique two-stage framework for mapping forested wetland areas. This framework effectively utilized multiple sources of remote sensing data and demonstrated the potential of remote sensing for identifying forest-wetland areas in the Changbai Mountain region. To the best of our knowledge, for the first time, we generated a forest swamp map with a resolution of 10 m for representative areas of the Changbai Mountains. The model achieved an average AUC of 0.89 through 10-fold cross-validation, indicating its excellent performance. The resulting map showed an overall classification accuracy of 87.18% and a Kappa coefficient of 0.84. The producer and user accuracies for forest swamp extraction were both notably high, reaching 80.37% and 86.87%, respectively.

This innovative methodology and the resulting forest-swamp products offer more accurate data support for wetland conservation and sustainable development in the Changbai Mountain region. Furthermore, this case study is valuable for mapping forest swamps in other regions.

Author Contributions: Conceptualization, J.L., Y.L. and R.J.; methodology, J.L. and W.Z.; software, J.L. and Y.L.; validation, R.J. and W.Z.; formal analysis, J.L. and R.J.; investigation, R.J.; resources, W.Z.; data curation, R.J.; writing—original draft preparation, J.L. and Y.L.; writing—review and editing, R.J. and W.Z.; visualization, J.L.; supervision, W.Z.; project administration, W.Z.; funding acquisition, W.Z. All authors have read and agreed to the published version of the manuscript.

Funding: This work was supported by the National Natural Science Foundation of China (U24A20585); the National Natural Science Foundation of China (42471093); the National Science and Technology Basic Resources Survey Project (grant number 2019FY101703).

Data Availability Statement: The original contributions presented in this study are included in the article. Further inquiries can be directed to the corresponding author.

Conflicts of Interest: The authors declare no conflicts of interest.

References

1. Wang, B.W.; Mu, C.C.; Wang, B. Carbon storage of a primary coniferous forested wetland ecosystem in the temperate Changbai Mountain of China. *Acta Ecol. Sin.* **2019**, *39*, 3344–3354. [CrossRef]
2. Zhang, S. Optimal planning algorithm of forest wetland tourism path based on GIS. *Discret. Math. Sci. Cryptogr.* **2018**, *21*, 393–397. [CrossRef]
3. Rask, H.; Schoenau, J.; Anderson, D. Factors influencing methane flux from a boreal forest wetland in Saskatchewan, Canada. *Soil Biol. Biochem.* **2002**, *34*, 435–443. [CrossRef]
4. Yang, Y.; Bian, H.; Yang, X. A review of forest wetland ecosystem service function and valuation. *Wetl. Sci. Manag.* **2017**, *13*, 61–64. [CrossRef]
5. Zhu, D.; Ni, H.; Cui, F. Progress in the Restoration of Degraded Forest Wetland Ecosystems in the Daxing'anling Forest Area. *Ter. Nat. Resour.* **2013**, *35*, 61–63. [CrossRef]
6. Song, F.; Su, F.L.; Mi, C.X.; Sun, D. Analysis of Driving Forces on Wetland Ecosystem Services Value Change: A Case in Northeast China. *Sci. Total Environ.* **2021**, *751*, 141778. [CrossRef]
7. Tiner, R.W., Jr. Use of high-altitude aerial photography for inventorying forested wetlands in the United States. *For. Ecol. Manag.* **1990**, *33*, 593–604. [CrossRef]
8. Brinson, M.M. *A Hydrogeomorphic Classification for Wetlands*; U.S. Army Engineer Waterways Experiment Station: Vicksburg, MS, USA, 1993.
9. Hogg, A.R.; Todd, K.W. Automated Discrimination of Upland and Wetland Using Terrain Derivatives. *Can. J. Remote Sens.* **2007**, *33* (Suppl. S1), S68–S83. [CrossRef]
10. Yan, T.T.; Bian, H.F.; Liao, G.X.; Sheng, L.; Zhang, J.; Gao, M. Research Status of Remote Sensing Information Extraction Methods for Forest Wetlands. *Remote Sens. Land Resour.* **2014**, *26*, 11–18. [CrossRef]
11. Lunetta, R.S.; Balogh, M.E. Application of Multi-Temporal Landsat 5 TM Imagery for Wetland Identification. *Photogramm. Eng. Remote Sens.* **1999**, *65*, 1303–1310.
12. Sader, S.A.; Ahl, D.; Liou, W.S. Accuracy of Landsat-TM and GIS Rule-Based Methods for Forest Wetland Classification in Maine. *Remote Sens. Environ.* **1995**, *53*, 133–144. [CrossRef]
13. Lin, Y.C.; Sarabandi, K. A Monte Carlo Coherent Scattering Model for Forest Canopies Using Fractal-Generated Trees. *IEEE Trans. Geosci. Remote Sens.* **1999**, *37*, 440–451. [CrossRef]
14. Kwoun, O.; Lu, Z. Multi-Temporal RADARSAT-1 and ERS Backscattering Signatures of Coastal Wetlands in Southeastern Louisiana. *Photogramm. Eng. Remote Sens.* **2009**, *75*, 607–617. [CrossRef]
15. Wang, J.F.; Mao, D.H.; Du, H.S.; Wang, Z.M. Mapping Swamps in Hani Wetland by Combining Sentinel-1/2 Satellite Images. *Wetl. Sci. Manag.* **2021**, *17*, 2–7.
16. Lang, M.W.; Kasischke, E.S.; Prince, S.D.; Pittman, K.W. Assessment of C-Band Synthetic Aperture Radar Data for Mapping and Monitoring Coastal Plain Forested Wetlands in the Mid-Atlantic Region, USA. *Remote Sens. Environ.* **2008**, *112*, 4120–4130. [CrossRef]
17. Cohen, J.; Lemmetyinen, J.; Ruiz, J.J. Detection of soil and canopy freeze/thaw state in the boreal region with L and C Band Synthetic Aperture Radar. *Remote Sens. Environ.* **2024**, *305*, 114102. [CrossRef]
18. Lemmetyinen, J.; Ruiz, J.J.; Cohen, J. Attenuation of radar signal by a boreal forest canopy in winter. *IEEE Geosci. Remote Sens. Lett.* **2022**, *19*, 1–5. [CrossRef]
19. Whitcomb, J.; Moghaddam, M.; McDonald, K.; Podest, E.; Kellndorfer, J. Wetlands Map of Alaska Using L-Band Radar Satellite Imagery. In Proceedings of the IEEE International Geoscience and Remote Sensing Symposium, Barcelona, Spain, 23–28 July 2007; pp. 2487–2490. [CrossRef]
20. Corcoran, J.; Knight, J.; Brisco, B.; Kaya, S.; Cull, A.; Murnaghan, K. The Integration of Optical, Topographic, and Radar Data for Wetland Mapping in Northern Minnesota. *Can. J. Remote Sens.* **2011**, *37*, 564–582. [CrossRef]
21. Xulu, S.; Mbatha, N.; Peerbhay, K.; Gebreslasie, M. Detecting Harvest Events in Plantation Forest Using Sentinel-1 and -2 Data via Google Earth Engine. *Forests* **2020**, *11*, 1283. [CrossRef]
22. Dong, D.; Wang, C.; Yan, J.; He, Q. Combining Sentinel-1 and Sentinel-2 Image Time Series for Invasive Spartina alterniflora Mapping on Google Earth Engine: A Case Study in Zhangjiang Estuary. *J. Appl. Remote Sens.* **2020**, *14*, 044504.
23. Samadzadegan, F.; Toosi, A.; Dadrass Javan, F. A Critical Review on Multi-Sensor and Multi-Platform Remote Sensing Data Fusion Approaches: Current Status and Prospects. *Int. J. Remote Sens.* **2025**, *46*, 1327–1402. [CrossRef]
24. Li, J.; Zhang, J.; Yang, C.; Liu, H.; Zhao, Y.; Ye, Y. Comparative Analysis of Pixel-Level Fusion Algorithms and a New High-Resolution Dataset for SAR and Optical Image Fusion. *Remote Sens.* **2023**, *15*, 5514. [CrossRef]
25. Pal, M. Random Forest Classifier for Remote Sensing Classification. *Int. J. Remote Sens.* **2005**, *26*, 217–222. [CrossRef]
26. Mutanga, O.; Adam, E.; Cho, M.A. High Density Biomass Estimation for Wetland Vegetation Using WorldView-2 Imagery and Random Forest Regression Algorithm. *Int. J. Appl. Earth Obs. Geoinf.* **2012**, *18*, 399–406. [CrossRef]

27. Whiteside, T.G.; Bartolo, R.E. Mapping Aquatic Vegetation in a Tropical Wetland Using High Spatial Resolution Multispectral Satellite Imagery. *Remote Sens.* **2015**, *7*, 11664–11694. [CrossRef]
28. Bansal, M.; Goyal, A.; Choudhary, A. A Comparative Analysis of K-Nearest Neighbor, Genetic, Support Vector Machine, Decision Tree, and Long Short-Term Memory Algorithms in Machine Learning. *Decis. Anal. J.* **2022**, *3*, 100071. [CrossRef]
29. Sheykhmousa, M.; Mahdianpari, M.; Ghanbari, H.; Mohammadimanesh, F.; Ghamisi, P.; Homayouni, S. Support Vector Machine Versus Random Forest for Remote Sensing Image Classification: A Meta-Analysis and Systematic Review. *IEEE J. Sel. Top. Appl. Earth Obs. Remote Sens.* **2020**, *13*, 6308–6325. [CrossRef]
30. Zhang, Y.; Bergeron, Y.; Gao, L.; Zhao, X.; Wang, X.; Drobyshev, I. Tree Growth and Regeneration Dynamics at a Mountain Ecotone on Changbai Mountain, Northeastern China: Which Factors Control Species Distributions? *Ecoscience* **2014**, *21*, 387–404. [CrossRef]
31. Yu, D.D.; Han, S.J. Ecosystem Service Status and Changes of Degraded Natural Reserves: A Study from the Changbai Mountain Natural Reserve, China. *Ecosyst. Serv.* **2016**, *20*, 56–65. [CrossRef]
32. Hou, M.Z.; Li, L.; Yu, H.; Jin, R.; Zhu, W. Ecological Security Evaluation of Wetlands in Changbai Mountain Area Based on DPSIRM Model. *Ecol. Indic.* **2024**, *160*, 111773. [CrossRef]
33. Lu, S.B.; Chen, Y.H.; Xu, W.L.; Zhu, W. Wetland Classification in the Changbai Mountain Nature Reserve. *J. Beijing Norm. Univ. Nat. Sci.* **2012**, *28*, 57–61.
34. Plank, S.; Jüssi, M.; Martinis, S.; Twele, A. Mapping of Flooded Vegetation by Means of Polarimetric Sentinel-1 and ALOS-2/PALSAR-2 Imagery. *Int. J. Remote Sens.* **2017**, *38*, 3831–3850. [CrossRef]
35. Sienaert, S. Usability of Sentinel-1 C-band VV and VH SAR Data for the Detection of Flooded Oil Palm. Master's Thesis, Lund University, Lund, Sweden, 2023.
36. Schwerdt, M.; Schmidt, K.; Ramon, N.T.; Alfonzo, G.C.; Doring, B.J.; Zink, M.; Prats-Iraola, P. Independent Verification of the Sentinel-1A System Calibration. *IEEE J. Sel. Top. Appl. Earth Obs. Remote Sens.* **2015**, *9*, 994–1007. [CrossRef]
37. Gierszewska, M.; Berezowski, T. On the Role of Polarimetric Decomposition and Speckle Filtering Methods for C-Band SAR Wetland Classification Purposes. *IEEE J. Sel. Top. Appl. Earth Obs. Remote Sens.* **2022**, *15*, 2845–2860. [CrossRef]
38. Liu, H.; Ren, H.; Niu, X.; Xia, P. Extraction of Cyanobacteria Bloom in Chaohu Lake Based on Sentinel-2 Remote Sensing Images. *Ecol. Environ.* **2021**, *30*, 146–150.
39. Truckenbrodt, J.; Freemantle, T.; Williams, C.; Jones, T.; Small, D.; Dubois, C.; Thiel, C.; Rossi, C.; Syriou, A.; Giuliani, G. Towards Sentinel-1 SAR Analysis-Ready Data: A Best Practices Assessment on Preparing Backscatter Data for the Cube. *Data* **2019**, *4*, 93. [CrossRef]
40. Du, C.; Ren, H.; Qin, Q.; Meng, J.; Zhao, S. A Practical Split-Window Algorithm for Estimating Land Surface Temperature from Landsat 8 Data. *Remote Sens.* **2015**, *7*, 647–665. [CrossRef]
41. Liu, Y.; Zhu, Q.; Liao, K.; Lai, X.; Wang, J. Downscaling of ESA CCI Soil Moisture in Taihu Lake Basin: Are Wetness Conditions and Non-Linearity Important? *J. Water Clim. Chang.* **2021**, *12*, 1564–1579. [CrossRef]
42. Wang, M.; Mao, D.; Wang, Y.; Xiao, X.; Xiang, H.; Feng, K.; Luo, L.; Jia, M.; Song, K.; Wang, Z. Wetland Mapping in East Asia by Two-Stage Object-Based Random Forest and Hierarchical Decision Tree Algorithms on Sentinel-1/2 Images. *Remote Sens. Environ.* **2023**, *297*, 113793. [CrossRef]
43. Kreft, I.G.G.; De Leeuw, J.; Aiken, L.S. The Effect of Different Forms of Centring in Hierarchical Linear Models. Multivar. *Behav. Res.* **1995**, *30*, 1–21. [CrossRef]
44. Feng, J.J.; Zhang, H.G.; Hu, X.J. The Scale Dependence of the Local Moran's I. *Stat. Appl.* **2015**, *4*, 162–168. [CrossRef]
45. Serneels, S.; De Nolf, E.; Van, E.P.J. Spatial Sign Pre-Processing: A Simple Way to Impart Moderate Robustness to Multivariate Estimators. *J. Chem. Inf. Model.* **2006**, *46*, 1402–1409. [CrossRef] [PubMed]
46. Mallick, J.; Talukdar, S.; Shahfahad; Pal, S.; Rahman, A. A Novel Classifier for Improving Wetland Mapping by Integrating Image Fusion Techniques and Ensemble Machine Learning Classifiers. *Ecol. Inform.* **2021**, *65*, 101426. [CrossRef]
47. Wu, F.; Ren, Y.; Wang, X. Application of Multi-Source Data for Mapping Plantation Based on Random Forest Algorithm in North China. *Remote Sens.* **2022**, *14*, 4946. [CrossRef]
48. Budiman, F. SVM-RBF Parameters Testing Optimization Using Cross Validation and Grid Search to Improve Multiclass Classification. *Sci. Vis.* **2019**, *11*, 80–90. [CrossRef]
49. Majnik, M.; Bosnić, Z. ROC Analysis of Classifiers in Machine Learning: A Survey. *Intell. Data Anal.* **2013**, *17*, 531–558. [CrossRef]
50. Fawcett, T. An Introduction to ROC Analysis. Pattern Recognit. *Lett.* **2006**, *27*, 861–874. [CrossRef]
51. Wang, Z. A New Clustering Method Based on Morphological Operations. *Expert Syst. Appl.* **2020**, *145*, 113102. [CrossRef]
52. Yang, Y.G.; Wang, X.J.; Zhang, L.D.; Jian, L.; Tao, S.; Yao, J.; Guan, L.; Gao, S.; Wang, T.; Xiong, X. A Method for Wetland Information Extraction and Ecological Sensitivity Evaluation Based on Microwave Remote Sensing and Optical Remote Sensing Technologies. CN Patent 107862255A, 23 April 2025.
53. Touzi, R.; Shimada, M.; Motohka, T. Calibration and Validation of Polarimetric ALOS-2 PALSAR-2. *Remote Sens.* **2022**, *14*, 2452. [CrossRef]

54. Liang, J.; Pan, J. Identifying Carbon Sequestration's Priority Supply Areas from the Standpoint of Ecosystem Service Flow: A Case Study for Northwestern China's Shiyang River Basin. *Sci. Total Environ.* **2024**, *927*, 172283. [CrossRef]
55. Bradley, A.P. The Use of the Area Under the ROC Curve in the Evaluation of Machine Learning Algorithms. *Pattern Recognit. Lett.* **1997**, *30*, 1145–1159. [CrossRef]
56. Xiang, H.; Yu, F.; Bai, J.; Shi, X.; Wang, M.; Yan, H.; Xi, Y.; Wang, Z.; Mao, D. SHAP-DNN Approach Advances Remote Sensing Mapping of Forested Wetlands. *IEEE J. Sel. Top. Appl. Earth Obs. Remote Sens.* **2025**, *18*, 6859–6869. [CrossRef]
57. Ali, A.M.; Darvishzadeh, R.; Shahi, K.R.; Skidmore, A. Validating the Predictive Power of Statistical Models in Retrieving Leaf Dry Matter Content of a Coastal Wetland from a Sentinel-2 Image. *Remote Sens.* **2019**, *11*, 1936. [CrossRef]

Disclaimer/Publisher's Note: The statements, opinions and data contained in all publications are solely those of the individual author(s) and contributor(s) and not of MDPI and/or the editor(s). MDPI and/or the editor(s) disclaim responsibility for any injury to people or property resulting from any ideas, methods, instructions or products referred to in the content.